Influence of aerosols on the life cycle of a radiation fog event. A numerical and observational study

S. Stolaki [a], M. Haeffelin [b,*], C. Lac [c], J.-C. Dupont [d], T. Elias [e], V. Masson [c]

[a] *Laboratoire de Météorologie Dynamique, École Polytechnique, 91128, Palaiseau Cedex, France*
[b] *Institut Pierre-Simon Laplace, École Polytechnique, 91128, Palaiseau Cedex, France*
[c] *CNRM/GAME, 42 Av. G. Coriolis, 31057, Toulouse Cedex, France*
[d] *Institut Pierre-Simon Laplace, Université Versailles Saint Quentin, 78280, Guyancourt, France*
[e] *HYGEOS, 165 Av. de Bretagne, 59000, Lille, France*

ARTICLE INFO

ABSTRACT

Despite the knowledge gained on the physical processes dominating the formation, development and dissipation of radiation fog events, uncertainties still exist about the role of the microphysical processes related to aerosol characteristics. The objective of this work is to analyze the sensitivity of fog to aerosols through their impacts on the fog droplets. A radiation fog event that formed on 15/11/2011 at the SIRTA Observatory near Paris in the context of the 2011–2012 ParisFog field campaign is the basis of this study. The selected case is one that initially forms a few hundred meters above the surface and within half an hour lowers down to the surface. A combination of SIRTA's sophisticated observations and 1D numerical simulations is employed with the aim of better understanding the influence of thermodynamics and microphysics on the life-cycle of the fog event and the degree to which aerosol characteristics such as concentration of potentially activated aerosols, size and solubility affect its characteristics. It results that the model simulates fairly well the fog life cycle, with only one half hour advance in the onset and one hour in the dissipation at the surface. The quality of the reference simulation is evaluated against several in-situ and remote sensing measurements. A numerical sensitivity analysis shows that the fog characteristics are strongly influenced by the aerosols. Doubling (halving) the cloud condensation nuclei (CCN) number translates into a 160% increase (65% decrease) in the production of fog droplets, and a 60% increase (40% decrease) of the liquid water path (LWP). The aerosols influence up to 10% the fog geometrical thickness. The necessity for more detailed local forcings that will produce better thermohygrometric conditions in the upper levels above the formed fog layer is underlined, as well as the addition of microphysical measurements in the vertical that will allow to improve two-moment microphysics schemes.

© 2014 Elsevier B.V. All rights reserved.

1. Introduction

Radiation fog, though one of the most extensively studied fog types, is still complex to fully understand and difficult to study. The efforts of the researchers in order to improve the knowledge of fog have been twofold: on one hand several observational studies have been carried out, while on the other hand the implementation of numerical models has been widespread. Throughout the years, several field campaigns in

* Corresponding author at: IPSL/LMD, École Polytechnique, 91128, Palaiseau Cedex, France. Tel.: +33 16933 5159.
E-mail addresses: sstavrou@lmd.polytechnique.fr (S. Stolaki), martial.haeffelin@ipsl.polytechnique.fr (M. Haeffelin), christine.lac@meteo.fr (C. Lac), jean-charles.dupont@ipsl.polytechnique.fr (J.-C. Dupont), te@hygeos.com (T. Elias), valery.masson@meteo.fr (V. Masson).

many countries and under different topographic and atmospheric characteristics have been held (Price, 2011; Roach, 1976, UK; Meyer and Lala, 1986, USA; Fuzzi et al., 1992, 1998, Italy; Duynkerke, 1999, Netherlands; Gultepe et al., 2009, Canada; Haeffelin et al., 2010, France; Liu et al., 2012, China; Román-Cascón et al., 2012, Spain). The findings of the campaigns and the rich source of data have significantly helped improve numerical simulation studies on fog physics. The latter concern the development and application of a variety of 1D (Guedalia and Bergot, 1994; Duynkerke, 1991; Bott et al., 1990; Musson-Genon, 1987; Fisher and Caplan, 1963) or 3D models (Shi et al., 2012; Cuxart and Jiménez, 2012; Müller et al., 2010; Van der Velde et al., 2010; Pagowski et al., 2004) for the study of fog. In particular, the application of single column models on fog studies allows for a computationally efficient and practical experimentation on the interaction among the different physical local processes (dynamic, thermodynamic, radiative, microphysical and chemical) that influence the fog life cycle and characterize its complex nature.

Despite the knowledge acquired so far, uncertainties still exist about the physical mechanisms and the interactions driving fog variability. In particular there is a need for further investigation on the aerosol interactions with microphysical processes in fog conditions. Intricate relationships exist between aerosols and fog characteristics since the activation and diffusion growth of droplets depend on the physicochemical character of the ambient aerosols (Gultepe et al., 2007). Activated aerosols which serve as activated CCN, exert a substantial influence on fog's supersaturation and, as a result, on fog formation. At the same time, their chemical nature, their amount and size determine the condensation at the fog onset, as well as the number and size of the droplets that will form. The aerosols' total number concentration, as well as their size and chemical composition may vary, depending on geographical location. Several works have been published concerning the interaction of aerosols and fog (Elias et al., 2014[1]; Elias et al., 2009; Rangognio et al., 2009; Lillis et al., 1999; Seinfeld et al., 1992; Bott and Carmichael, 1993; Bott, 1991; Eldridge, 1966) underlining their influence on fog life cycle.

The number concentration of activated CCN largely determines the cloud droplet number concentration and indirectly influences the liquid water content of fog. Therefore the aerosols' activation mechanism is rather critical affecting the formation of fog and its further development. Much about the aerosol activation process is understood quite well (Pruppacher and Klett, 1997), but the complete aerosol activation theory is complex. The parameterization of activation must account for the competition between aerosol particles and for the dependence of the competition on particle size and distribution, on their chemical nature and solubility, as well as on the supersaturation forcing rate. Squires (1958), Twomey (1959) and

Squires and Twomey (1960) developed analytical expressions that relate the total number of activated aerosols to supersaturation and, in essence, to vertical velocity. The most important deficiency of such expressions is that they are not bound by the total aerosol number, therefore errors arise. Moreover they do not relate the activation spectrum to aerosol characteristics such as their size and chemical composition. Cohard et al. (1998) corrected this weakness by introducing a more general description of the activation spectra that determines the sensitivity of the activation spectra to microphysical characteristics of aerosols (concentration, size, solubility) and air temperature, through four adjustable parameters. On the other hand, the parameterization of Abdul-Razzak et al. (1998) uses a lognormal representation of the aerosol size distribution, considering two different aerosol growth regimes. For the approximate and asymptotic solutions of these two regimes a first-order interpolation between them is applied. It has been extended to a multimode version by Abdul-Razzak and Ghan (2000).

This work presents an effort to highlight the physical processes that take place during the life cycle of a radiation fog event that occurred at the SIRTA Observatory (48.718° North, 2.208° East, 156 m above mean sea level), near Paris, in France, on 15 November 2011 and during the ParisFog field experiment campaign of the winter 2011–2012. One of the special features of this fog event is the fact that aerosols are activated to form droplets at a higher level above surface, as a result of vertical mixing inducing sufficient adiabatic cooling of the air parcel in updraft to reach supersaturation conditions at that level, while supersaturation conditions are not reached at the surface. The approach followed is that of combining sophisticated measurements of various thermohygrometric, radiative, dynamical and microphysical parameters, in order to understand the fog event itself, with a 1D modeling tool that highlights processes that are essentially difficult to examine through measurements. The ultimate objective of this work is to quantitatively examine the influence of the aerosols characteristics such as their total number concentration and chemical nature on the radiation fog life cycle with a particular emphasis on features of the fog layer, such as height and density. This task is accomplished by focusing on the mechanism of the CCN activation that further gives the activation spectra of aerosols. This mechanism is parameterized in the numerical model and it is here adjusted to conform to the aerosol conditions prevailing at SIRTA before the fog occurrence. Numerical tests with the numerical model are conducted in order to examine the model's sensitivity to the aerosol characteristics mentioned earlier as far as the fog life cycle is concerned. For the current study, the CCN activation parameterization of Cohard et al. (1998) is applied.

Section 2 provides a description of measurements and the numerical tool and its configuration used in the study, the description of the aerosol activation parameterization scheme applied, as well as the configuration set up of the reference run used for the sensitivity tests. In Section 3, the fog case under study is analyzed concerning all the physical processes that take place during the formation, development and dissipation stages of the event as recorded at SIRTA. Section 4 focuses on the examination of the model's performance regarding thermohygrometric, radiative, dynamical and microphysical features

---

[1] Elias, T., Jolivet, D., Dupont, J.-C., Haeffelin, M., Burnet, F., Hammer, E., 2014. Aerosols affecting the radiative budget during the fog life cycle: microphysical properties and extinction coefficient. Under review in Atmos. Res.

and presents the analysis of the sensitivity tests regarding the role of the aerosols total number concentration and chemical characteristics, as well as their impact on the fog life cycle. Conclusions are presented in Section 5.

2. Data and methods

2.1. Measurements used in the study

At SIRTA, the thermohygrometric, radiative, dynamical and microphysical processes driving the fog life cycle are fully monitored near the surface and throughout the boundary layer (Haeffelin et al., 2010). The site where the instrument platform is installed is a semi-urban area of a complex terrain consisting of a forest, a lake, meadows and shrubs next to an urban agglomeration. The case of interest is chosen from the SIRTA ParisFog database covering the 2010–2012 period that includes thirty-four radiation fog events. The ParisFog database consists of detailed measurements of thermohygrometric, dynamic, radiative, atmospheric properties observed at the surface with in-situ sensors and in the boundary layer using remote sensing instruments. The database also contains measurements of aerosol and liquid droplet microphysics near the ground.

At the surface, temperature and humidity non-aspirated sensors located between 1 and 30 m height on an instrumented mast provide the thermohygrometric measurements (with 0.2 °C uncertainty for temperature and 2% for relative humidity). Wind speed is measured by two Metek ultrasonic anemometers at 10 m and at 30 m agl installed on the same meteorological mast. The radiosonde profiles that are used are those performed routinely at 00 and 12 UTC, 15 km west of SIRTA as part of the Météo-France national network (with 0.2 °C uncertainty for temperature and 2% for relative humidity). Radiative flux is measured on a building roof and on a meteorological mast. Shortwave and longwave downwelling and upwelling flux are also measured at 30 m agl along a mast, with a 5 Wm^{-2} and 4 Wm^{-2} uncertainty, respectively. A Degreanne DF20+ diffusometer is operated near the ground (3 m agl) and a second Degreanne DF20 diffusometer is operated at 18 m agl providing information on the vertical heterogeneity of visibility during the fog life cycle with a ±10–25% uncertainty. The remote sensing instruments deployed for the ParisFog campaign and used in this study consist of a Vaisala CL31 ceilometer whose backscatter signal provides the cloud-base height. An RPG-HATPRO water vapor and oxygen multi-channel microwave profiler provides time series of LWP when fog occurs (with 0.2 gm^{-2} uncertainty). Wind is measured by a Leosphere Doppler wind lidar (WLS7v2) for horizontal wind profiles between 40 and 200 m and vertical velocity (air velocity in clear air and droplet vertical velocity when fog is present). A Remtech PA2 sodar for wind profiles between 50 and 600 m is also employed, with uncertainty equal to 0.3 ms^{-1}. Measurements of aerosol and liquid droplet microphysics near the ground come from a DMT Fog-Monitor 100 that provides size distributions of aerosols and droplets in ambient (i.e. air samples in the natural moist environment) conditions from 2 μm to 50 μm and liquid water content (LWC), while a TSI Scanning Mobility Particle Sizer (SMPS) measures dry aerosol spectra between 10.6 and 496 nm every 15 min.

2.2. Meso-NH model and set up

Meso-NH is a 3D non-hydrostatic, pseudo-compressible research model jointly developed by CNRM/GAME and the Laboratoire d'Aérologie (Lafore et al., 1998), intended for the study of meteorological mesoscale and microscale phenomena. Meso-NH, either in its 3D meso-scale mode (Cuxart and Jiménez, 2012), in 1D mode (Bergot et al., 2007) or in the configuration of large-eddy simulation (LES) modeling (Bergot, 2012) has been used in several research efforts in order to study and understand fog processes. In the current study the 1D mode is applied with the ultimate goal of focusing on the examination of the individual and combined role that processes related to aerosol microphysics play during the fog life cycle. It uses a 2-moment warm microphysics scheme (Geoffroy et al., 2008; Khairoutdinov and Kogan, 2000). Droplet sedimentation is applied to the cloud droplet number concentration and the mixing ratio, as it is essential so that to reproduce the fog life cycle (Bergot et al., 2007). It is parameterized by assuming a Stokes law to calculate the cloud droplets terminal velocity, including an air density effect (Foote and Toit, 1969) and by assuming an analytical distribution to represent the cloud droplet spectra. The analytical distribution used is a generalized gamma law. Turbulence is parameterized according to Cuxart et al. (2000) with the Bougeault and Lacarrére (1989) mixing length. Radiation is parameterized with the ECMWF radiation scheme code (http://www.ecmwf.int/research/ifsdocs/CY23r4/). Details of the short-wave radiation code are given in Morcrette (1991), while the longwave radiation scheme used is the Rapid Radiation Transfer Model (RRTM, Mlawer et al., 1997). The three-layered soil-vegetation scheme ISBA (Interactions between the Soil Biosphere and Atmosphere, Noilhan and Planton, 1989) is applied. 131 vertical levels are used between the surface and the top of the model at 5000 m, with 126 levels between the ground and 1500 m and a vertical resolution less than 1 m in the first 200 m above ground level.

The model has been initialized at 12 UTC on 14 November 2011 and the simulation covers the following 24 h. For all simulations performed, temperature, humidity and wind speed vertical profiles are initialized with data derived from the radiosonde launched by Météo-France in TRAPPES (48.7°N, 2°E). The wind speed is modified near the ground with the data recorded at a 30 m meteorological mast at the SIRTA site. Trappes is located in the western suburb of Paris (15 km west of SIRTA) and can differ slightly from the SIRTA site for the meteorological conditions. The forcings are deduced from the radiosondes and they consist of a prescribed geostrophic wind of 6.5 m s^{-1} which remains constant in time and height for the entire simulation. A small subsidence of 0.45 cm s^{-1} has been introduced for the first 12 h. Finally, a moisture advection of 10^{-5} g kg^{-1} s^{-1} constant in the vertical is introduced in the last 12 h of the simulation.

The time step is 10 sec and the radiation scheme is called every 1 min. Soil temperature (in K) and soil moisture (in %) data for three layers (surface, root zone and deep soil) have also been imposed at the initialization of the model corresponding to observed ones at SIRTA. The surface cover is composed of 70% of temperate pastures, 20% of temperate suburban and 10% of river surface types. For all the tests performed the aforementioned configuration has been employed.

2.3. The CCN activation scheme

According to Cohard et al. (1998), Cohard and Pinty (2000), the activated CCN number concentration is expressed by:

$$N_{CCN} = CS^k_{max} F\left(\mu, \frac{k}{2}, \frac{k}{2} + 1; -\beta S^2_{max}\right) \qquad (1)$$

where S_{max} is the maximum supersaturation estimated using the following equation:

$$S^{k+2}_{max} F\left(\mu, \frac{k}{2}, \frac{k}{2} + 1; -\beta S^2_{max}\right) = \frac{(\psi_1(T,P)w)^{3/2}}{2kc\pi\rho_w\psi_2(T,P)^{3/2}B\left(\frac{k}{2}, \frac{3}{2}\right)} \qquad (2)$$

while C is proportional to the total number concentration of CCN (activated aerosols) that would be activated when supersaturation S_{max} tends to infinity. Parameters k, μ and β are adjustable shape parameters associated with the characteristics of the aerosol size spectrum such as the geometric mean radius ($\bar{r}$) and the geometric standard deviation (σ), as well as with chemical composition, solubility of the aerosols (ϵ_m) and temperature (T). $\psi_1(T)$ and $\psi_2(T,P)$ are functions of temperature and pressure. B(a, b) and F(a, b; c; x) are the Beta function and the Hypergeometric function, respectively. The parameter w is the vertical velocity.

Cohard et al. (2000) show that it is possible to establish parametric relations between the unknowns k, β and μ in (1) and characteristics of lognormal distributions of underlying aerosols with variable chemical composition and solubility. Two chemically pure aerosol types are taken into account in their study, the continental and the maritime. For the continental case the ammonium sulfate is considered, while for the maritime sea salt. In this way, the scheme in essence differentiates between more numerous and less soluble (continental) aerosols versus less numerous, coarser and more soluble (maritime) particles. For both cases, the values of all of these parameters are given in Cohard et al. (2000).

In order to reconstruct the supersaturation spectrum for the SIRTA conditions and further study the influence of aerosol characteristics on fog, it is necessary to determine the size distribution parameters (geometric mean radius, the natural logarithm of the geometric standard deviation) of the aerosols, their concentration, the solubility and the temperature of the air mass near the surface. The values of these parameters will provide the values of C, k, β and μ. Therefore the challenge comes down to representing as realistically as possible the inherent local aerosol characteristics of the air mass close to the surface and around the time of the fog formation. Here the continental aerosols are considered. In order to define the exact values of the statistics parameters (aerosol total number concentration, geometric mean radius and geometric standard deviation), fitting tests of aerosol size distribution on 15 min frequency data of aerosol number concentration from the SMPS for the 14 and 15 November 2011 were performed. Log normal distributions of two or three modes were fitted to the data and sensitivity tests of the model have been made in order to define the most appropriate set of the two statistics parameters for a satisfactory simulation of the fog event. The outcomes of this effort are described in the following section.

2.4. Reference run

For the model analysis of the fog event presented in this work, a reference run regarded as the control simulation was performed. The performance of the model is examined based on this run, while this run is also the basis on which the sensitivity tests on the total aerosol number concentration and aerosol solubility are performed. For the control simulation the statistics of the trimodal fitted distribution of the SMPS data of 0215 UTC, 15/11/2011 was used (Fig. 1). It should be noted that in the model the aerosol characteristics and their chemical composition are not altered with time. Therefore we selected this time point because it corresponds to representative aerosol conditions at the time of initial fog formation and it is these aerosols that will serve as CCN for the formation of the fog droplets. Table 1 presents the values of the concentration of the number of CCN that can be potentially activated (N), the geometric mean radius ($\bar{r}$), the geometric standard deviation (σ) and its natural logarithm (lnσ) for the three fitted modes: nucleation, Aitken and accumulation. Since in Meso-NH a single aerosol mode is represented, only the accumulation mode is considered. Recent observations at SIRTA indicate that only aerosols larger than 200 nm tend to activate under typical conditions favoring radiation fog formation (Hammer, personal communication). The other two modes correspond to sizes much smaller than this threshold. Air temperature at 2 m was set equal to 2.3 °C as it corresponds to the 2 m SIRTA's meteorological mast temperature at 0215 UTC of 15/11/2011. Solubility was set equal to 0.4 because according to aerosol chemical speciation measurements, only 40% of aerosols are hydrophilic. Further explanations are provided in Section 4.3.2.

3. Description of the case studied

The selected fog event formed at 02 UTC of 15 November 2011 and dissipated after 7.5 h, at 0930 UTC. According to the
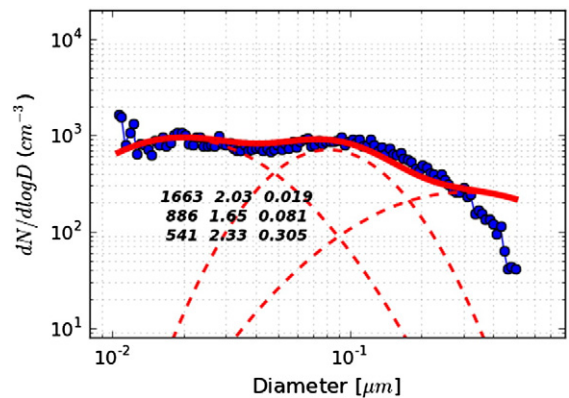

Fig. 1. Trimodal fit to the SMPS data of 15/11/2011 at 0215 UTC. The numbers from left to right correspond to the CCN number concentration (N, #m^{-3}), the geometric standard deviation (σ) and the geometric mean diameter (D, μm) for each of three modes: nucleation, Aitken and accumulation.
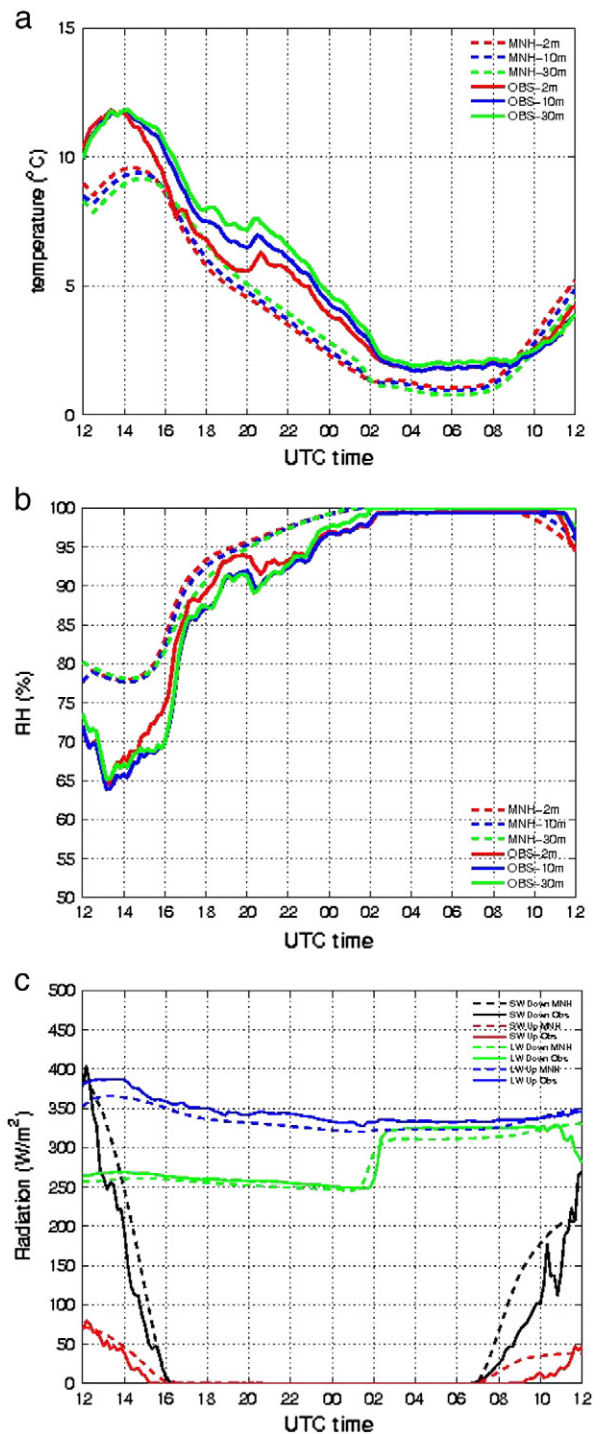
Table 1
Values of the CCN number concentration (N), the geometric mean radius ($\overline{r}$), the geometric standard deviation (σ) and its natural logarithm (lnσ) for the three fitted modes for 0215 UTC of 15/11/2011.

CCN number concentration N (#cm^{-3})	geometric mean radius $\overline{r}$ (μm)	geometric standard deviation σ	lnσ
1663	0.0095	2.03	0.71
886	0.0405	1.65	0.50
541	0.1525	2.33	0.85

classification of fog events applied at SIRTA (based on the Tardif and Rasmussen (2007) classification method), this is a typical radiation fog event frequently forming over this area. Moreover, as described in the following sections, this is an elevated radiation fog event, characterized by radiative cooling conditions at the surface followed by the formation of a cloud layer 100–200 m agl, followed shortly by fog at the surface. This characteristic is common for radiation fogs occurring in November since 88% of the radiation fog events formed at SIRTA during the three campaign periods (2010–2011, 2011–2012, 2012–2013) are also elevated. Fog events at SIRTA pertaining to the radiation category usually form during the night and over half of them dissipate 2 h after sunrise (Dupont et al. 2014, under review[2]). Moreover this is a fog event that produced low LWC near the surface (up to 0.04 gm^{-3}). The average 2.5 m LWC of the radiation fog events formed over the 2011–2012 season is 0.037 gm^{-3} (standard deviation 0.013 gm^{-3}). Also the synoptic and near surface meteorological conditions prevailing during the evening of 14 November 2011 were typical for the formation of such a fog type. According to the synoptic conditions of 14 November 2011, at the 500 hPa level (12 UTC), a ridge, centered over the North Sea, was affecting northern France. At the surface, these upper level conditions were associated with an anticyclone with high pressures over France. At SIRTA, such synoptic conditions favored the absence of low and middle clouds between 18 UTC (14/11/2011) and 02 UTC (15/11/2011).

3.1. Daytime conditions before the fog event (12–16 UTC)

Near-surface temperature measurements (2–30 m agl) shown in Fig. 2a reveal a diurnal cycle typical of a clear, relatively mild fall day, with a maximum temperature of 12 °C near 14 UTC on 14/11/2011. The near surface relative humidity (RH) (Fig. 2b) at noon dropped to about 65%. According to the diurnal cycle of the surface solar (short-wave, SW) and thermal (longwave, LW) irradiances (Fig. 2c), the net SW irradiance peaked near 12 UTC with a net value of about +325 Wm^{-2} and sharply decreased to +100 Wm^{-2} at 14 UTC and 0 Wm^{-2} at 16 UTC. The net LW irradiance peaked at about −150 Wm^{-2} at 12 UTC, and stabilized near −90 Wm^{-2} after sunset (−75 Wm^{-2} at 00 UTC). Such strong near-surface radiative cooling conditions are typical of cloud-free low-humidity conditions.

---

[2] Dupont, J.-C., Haeffelin, M., Stolaki, S., Elias, T., Burnet, F., Sciare, J., 2014. Analysis of physical processes driving fog and quasi-fog life cycle: Statistical analysis during the ParisFog field experiment. Under review in Pure and Applied Geophysics.


Fig. 2. Observed and simulated 24-h time series of (a) temperature and (b) relative humidity at 2 m, 10 m and 30 m agl height, and (c) downward (at 17 m) and upward (at 30 m) shortwave and longwave radiation. Simulation initialized at 12 UTC, 14/11/2011. Observed fog formation: 02 UTC; observed fog dissipation: 0930 UTC.

Fig. 3a shows a 24-h time series of CL31 ceilometer vertical profile (0–600 m agl) of un-calibrated attenuated backscatter power in logarithmic scale. Backscattered power

at 905 nm in cloud free skies is predominantly due to aerosol scattering, but is also affected by water vapor absorption. When liquid water is present in the atmosphere, the droplet cross section dominates scattering and the ceilometer power can be extinguished by a 100-m deep liquid layer. Cloud base heights derived with the STRAT algorithm (Morille et al., 2007) are shown with green dots. Boundary layer height, shown as black squares, are derived with the STRAT + algorithm (Pal et al., 2013) using the vertical profile of attenuated backscatter at 355-nm measured by a Leosphere ALS450 Lidar and surface stability

conditions associated with Obukhov lengths derived from sonic anemometer measurements. Fig. 3a confirms that the atmosphere is cloud-free between surface and 600 m agl from 12 UTC to 02 UTC. Fig. 4a shows the vertical profile of vertical wind speed and Fig. 4b the temperature structure parameter, a proxy for turbulence, as derived from the Remtech PA2 Sodar. During daytime, the wind was southeasterly and less than 4 ms^{-1} inside the mixing layer, while it was southwesterly and about 8 ms^{-1} above the boundary layer. Significant wind shear occurred near the top of the boundary layer.
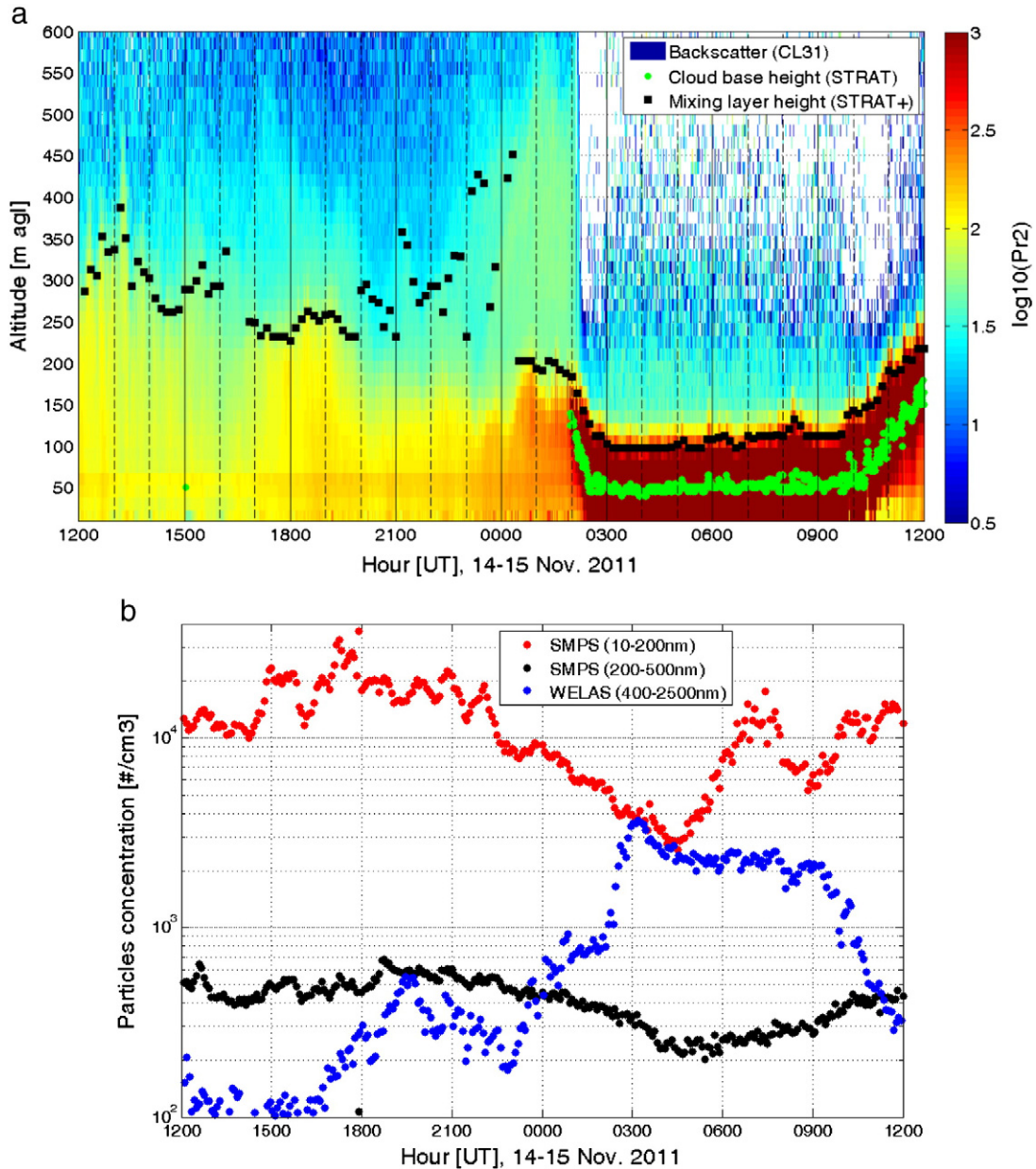
Fig. 3. (a) 24-h time series of vertical profile of un-calibrated attenuated backscatter power measured by a CL31 ceilometer (logarithmic color scale), cloud base height (green dots), and mixing layer height (black dots); (b) time series of aerosol number concentration near the surface provided by the SMPS (red dots = 10–200 nm aerosol dry diameter range; black dots = 200–500 nm diameter), and by the Welas (blue dots = 400–2500 nm aerosol diameter range in ambient conditions); (c) hygroscopic growth function of ceilometer backscattering coefficient as a function of relative humidity.
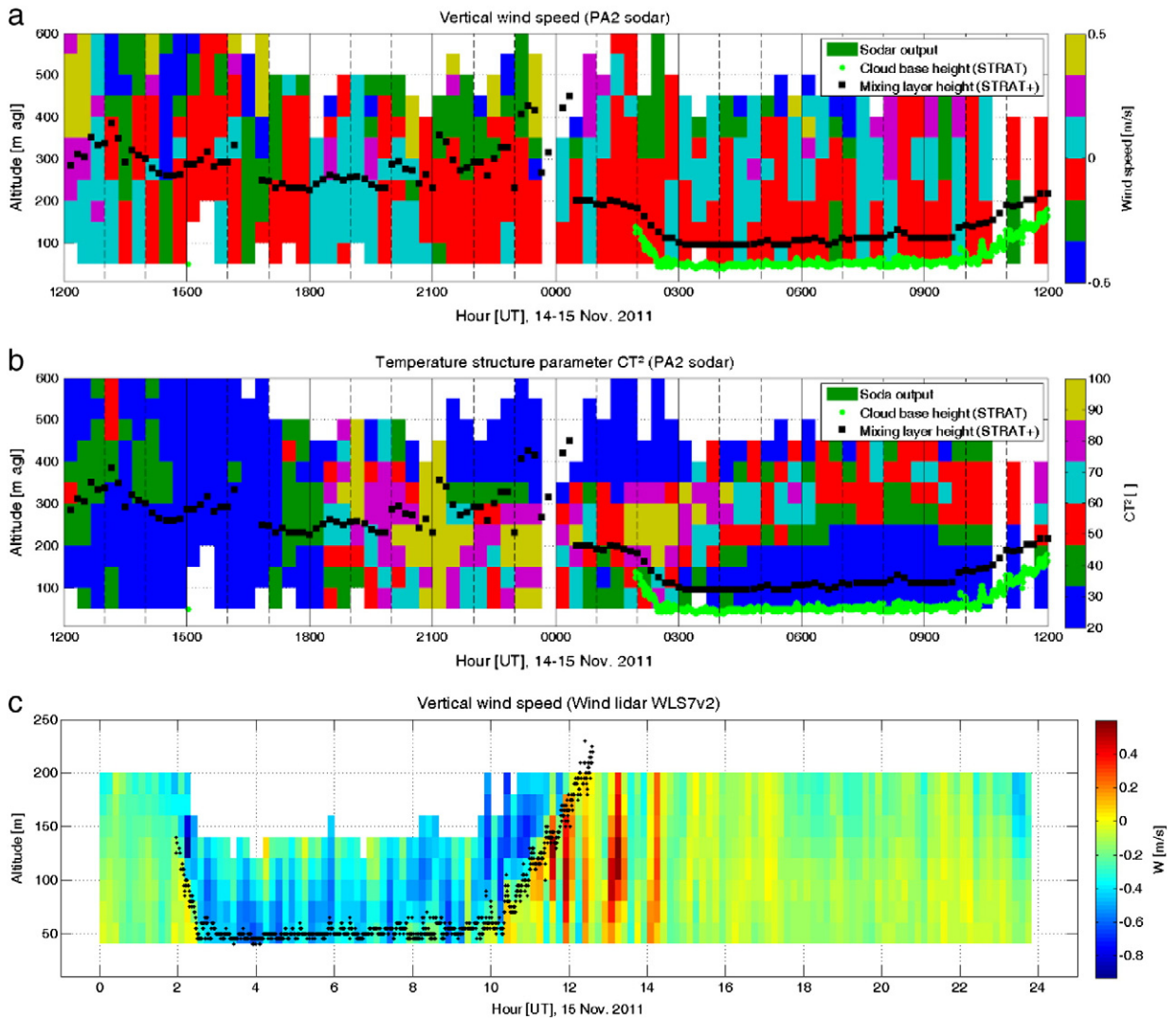
Fig. 4. (a) Vertical profile of vertical wind speed (ms⁻¹); (b) vertical profile of temperature parameter CT2; both measured by Remtech PA2 sodar. Cloud base height shown in red dots, mixing layer height shown in black squares; (c) vertical profile of vertical wind speed (ms⁻¹) measured by Leosphere WLS Doppler Lidar. Cloud base height derived from the ceilometer is shown in black squares.

3.2. From sunset to aerosol activation (16–02 UTC)

After sunset, under clear conditions, the net radiative balance at the surface reached −90 Wm⁻². Surface cooling conditions remained at that level for 10 h from 16 to 02 UTC. Under moderate wind conditions at the surface (about 2 ms⁻¹), this triggered a long and gradual cooling of the near-surface layer at an average cooling rate of −0.8 °C/h (Fig. 2a). The wind speed (not shown) increased in the boundary layer after 17 UTC, reaching values of 8 ms⁻¹. The combination of mechanical mixing and surface radiative cooling induced cooling in the lowest 300-m above the ground (not shown). The boundary layer became stable soon after sunset (16 UTC), reaching a lapse rate of 0.03 °Cm⁻¹ over the lowest 300 m. Similarly the RH near the surface increased sharply from 16 to 18 UTC at +9% per hour, followed by a moderate increase of about +1% per hour for the

next 8 h until 02 UTC on 15/11/2011. This rapid increase was also observed throughout the 300-m deep boundary layer.

Between 18 and 21 UTC, the horizontal wind speed increased sharply and veered Easterly above the boundary layer (not shown). This affected also the wind speed inside the boundary layer, with wind speed greater than 8 ms⁻¹ at 100 m agl, and greater than 12 ms⁻¹ at 200 m agl after 19 UTC. Such wind conditions indicate the existence of a low level jet above the boundary layer which, between 21 and 00 UTC, propagated from the free troposphere into the boundary layer, as also evidenced by the negative values of the vertical wind speed (−0.1 ms⁻¹). Turbulence in and above the boundary layer increased suddenly inducing mixing of air from ground to 600 m agl. The temperature increased 1–2 °C throughout the boundary layer while it was cooling rapidly before 18 UTC (Fig. 2a). According to microwave

brightness temperature measurements (not shown) there is evidence that this resulted from mixing of warmer air from a layer at 350–850 m agl into the lower altitudes.

Between 21 and 00 UTC, the near-surface layer and boundary layer resumed a cooling trend, similar to that observed before 18 UTC (Fig. 2a). Similarly, the near-surface RH resumed an increasing trend, reaching values near 95% close to the surface at 23 UTC (Fig. 2b), and near 90% in the first 100-m above ground (not shown). Between 00 and 0130 UTC, the RH below (at 30 m agl) remained nearly constant at 97%. During this time interval, the wind speed in the boundary layer stabilized around 6 ms^{-1}, while near the surface was light (around 1.9 m^{-1}) and the vertical wind speed was mostly positive at about $+0.2$ ms^{-1}.

3.3. Fog onset and development (02–07 UTC)

At 02 UTC, the attenuated backscatter coefficient at 150 m agl increased by a factor of 10, due to formation of droplets at that altitude (Fig. 3). It is likely that aerosols near 150 m agl activated to form droplets as a result of vertical mixing inducing sufficient adiabatic cooling of air parcels in updrafts to reach supersaturation conditions at 150 m agl. Supersaturation conditions were not reached at the surface as RH remained at 97% (Fig. 2b). The upwelling LW irradiance at the top of the cloud layer was probably between 280 and 350 Wm^{-2}, given the cloud top temperature was about 280 K and considering a cloud emissivity evolving from 0.8 towards 1 as the LWP increased between 02 and 03 UTC. The downwelling LW irradiance at 200 m agl was likely about 200 Wm^{-2}, as the humidity dropped sharply above 200 m agl. The radiative cooling at the top of the liquid layer evolved hence from about -80 to -150 Wm^{-2}. This is a typical value when the atmosphere is dry aloft (Dupont et al., 2012; Philipona et al., 2013), while a typical radiative cooling value just above the surface is on the order of -60 to -80 Wm^{-2}.

After the liquid layer formed at 150 m agl, the cloud base height progressively subsided during about 30 min, until it reached the ground (Fig. 3). During this subsidence, the temperature in the surface layer continued to decrease by about 1 °C, while the RH quickly reached 100%. Before 02 UTC, the cooling of the surface layer was due to a negative radiative budget at the surface (about -80 Wm^{-2}). After 02 UTC, the cloud layer at 150 m agl quickly increased the downwelling longwave radiative flux at the surface resulting in a near 0 Wm^{-2} surface radiative budget. Hence the temperature decrease resulted from another cooling process. As described in Dupont et al. (2012), at 02 UTC, radiative cooling at the top of the cloud layer cooled the air at the top of the cloud and destabilized the cloud layer, inducing vertical mixing in the cloud layer. Fig. 4c (vertical speed measured by a Doppler Lidar) shows that during this phase, cloud droplet sedimentation in the cloud layer reached a rate of -0.2 to -0.6 ms^{-1}. In clear air, the Doppler Lidar traces vertical air motion (aerosols serve as tracers), while in the cloud, the Doppler signal is dominated by the vertical motion of cloud droplets. Droplets evaporate below cloud base before they reach the ground, and hence cool the sub-cloud layer. This cooling effect destabilizes the sub-cloud layer, leading to efficient coupling with the surface. Hence the surface layer is cooled from the top. This mechanism is fast as evidenced by the temporal evolution of near-surface visibility, which

dropped from 5 to 1 km in about 30 min (not shown). In a typical radiation fog this process takes two to four times longer (Haeffelin et al., 2013).

Once the cloud layer reached the ground layer, the visibility at 18 m agl stabilized around 200 m while the visibility at 3 m agl hovered near 400 m. Hence the liquid water content was not homogeneous in the vicinity of the surface. The LWP (Fig. 6a) of the fog grew quickly after 0230 UTC to 30 gm^{-2} and continued to increase continuously until sunrise, reaching a maximum value of nearly 75 gm^{-2} at 07 UTC. The fog top height also increased from 150 m agl at 0230 UTC to reach a maximum height of 300 m agl, as shown by the Sodar turbulence parameter (CT2) which is maximum at fog top where strong radiative cooling induces turbulence (Dabas et al., 2011).

3.4. Fog dissipation (07–10 UTC)

Sunrise occurred at 07 UTC precisely. About one hour after sunrise, between 0745 and 0845 UTC, the wind speed at 10 m agl increased from 2 to 3.5 ms^{-1} (not shown) and mean vertical air velocity became positive ($+0.2$ ms^{-1} at 200 m agl, Fig. 4a). As the air lifted, the fog droplet fall velocity (Fig. 4c) was reduced. This resulted in an increase of visibility peaking at 2 km (not shown). This mixing and lifting motion lasted only one hour, and the cloud base subsided back to the ground at 09 UTC. At 10 UTC, the downwelling SW irradiance exceeded 100 Wm^{-2}, while near-surface temperature had increased by 1 °C compared to pre-sunrise values. This created enough buoyancy to offset the droplet fall velocity and to produce the rise of the fog base height. Vertical air velocity reached $+0.5$ ms^{-1} below cloud base (Fig. 4c) and the cloud base rose at a rate of about 75 mh^{-1}. This fog dissipation occurred through a classic scenario of heating the fog layer from below due to absorption of solar radiation by the surface after sunrise (0659 UTC).

4. Simulation results

In order to better understand the model's behavior in simulating the fog event under study, the performance of a control simulation is examined. Such an examination is based on comparisons between observed and modeled values of thermo-hygrometric, dynamic, radiative and microphysical parameters spatially in the vertical and temporally during the 24 h simulation. Next, the model's sensitivity to CCN concentration, size distribution and solubility is studied. For all comparisons and sensitivity tests the reference run described in Section 2.4 is considered.

4.1. Thermohygrometric, radiative and dynamic performance of the model

This section describes the examination of the thermo-hygrometric, radiative and dynamic performance of Meso-NH. At first we compare the time series of surface (from 1 m to 30 m agl) temperature and RH and surface radiative fluxes for the duration of the simulation and next we compare the modeled and observed time series of TKE, as well as the vertical

profiles of wind speed every two hours between 22 UTC of 14/11/2011 and 10 UTC of 15/11/2011.

It is evident (Fig. 2a and b) that, almost throughout the entire simulation, the model underestimates the air temperature and, consequently, overestimates the RH near the surface. These biases are present from the beginning of the simulation and can be mainly attributed to the difference between Trappes, the location of the radiosonde used to provide the initial conditions for the simulation, and the SIRTA site. For temperature this underestimation reaches up to 4 °C before fog formation, while during the fog event it reaches 1 °C. Just after the beginning of the simulation the model produces a negative vertical temperature gradient, while the lower layer is isothermal in the observations. Therefore, the thermal inversion near the surface (T30-T1m agl difference) that forms several hours before fog formation appears with almost 2 h delay in the modeled values (at 16 UTC) than compared to the observed values (at 1410 UTC), and it is stronger in reality than in the simulated conditions (Fig. 2a). At all mast levels, between 20 and 2030 UTC, an increase of temperature that reached 0.8 °C (at 1 m agl height) is observed. This increase is more pronounced in the lower levels (1–2 m agl) and it is combined with a slight decrease of RH observed at the same levels. The vertical mixing of warmer air from the 600 m agl height down to the surface, around the same time that the temperature increase is observed and as described in Section 3.2, might be a possible reason for such a temperature increase. However an advection of warm air near the surface cannot be excluded and this might be the strongest influence for a near surface warming at the time. On the other hand in the modeled situation, the temperature at all levels continues decreasing. This happens due to the fact that in the model configuration only the large scale effects are considered in the forcings therefore the local effects cannot be precisely simulated. Since this heating effect through subsidence was not measured precisely, it could not be introduced as a forcing condition. During the fog event the model simulates a fog layer that is colder than the observed one up to 1 °C. But similar to reality, the layer is neutral, since temperature at all levels is almost the same. Coherently with temperature, for the first 4 h of the simulation, the modeled RH (Fig. 2b) overestimates the observed one by as much as 13% but after that the values differ less, although exceeding the uncertainty of the instrument (2%). However, observed RH reveals several deviations and fluctuations that are not represented by the model due to the simplified forcings. The air near the surface becomes saturated around half an hour earlier than observed. The simulated RH remains close to 100% up to around 10 UTC of 15/11/2011, similar to the observed conditions. Therefore despite some discrepancies in the thermodynamic conditions, the fog life cycle is fairly well reproduced.

Simulated and observed radiative fluxes show also a correct agreement throughout the period (Fig. 2c). The increase of the observed downwelling LW radiative flux at 17 m agl, occurring at the formation of the fog layer, appears simultaneously in the model. However, the increase is slightly underestimated by the model (60 Wm^{-2} instead of 75 Wm^{-2}). In the same manner, after sunrise (0659 UTC), the downward and upward SW fluxes are overestimated. Both

discrepancies indicate that the LWP is underestimated, a fact that is presented in Section 4.2. On the contrary, at the end of the simulation, the modeled infrared downward radiation remains large, in contrast to the observed one that after the end of the event (10 UTC) begins decreasing. In parallel, the downward SW flux is underestimated by the same amount indicating that the LWP is overestimated in the low level cloud to which the fog layer is transformed after the fog dissipation and up to the end of the simulation.

The dynamical performance of the model is examined through the study of TKE at 10 m agl and wind speed profiles (Fig. 5). The evolution of the TKE for the model and observations (Fig. 5a) shows that Meso-NH reproduces the general pattern for the changes in TKE variability but not in every detail. The first 4 h of the simulation, the model overestimates TKE and specifically at the onset of the event, when a small increase is observed. After 16 UTC and before the fog formation, TKE reaches equilibrium and it is close to reality. During the event the modeled TKE is less than half of the observed one. The increase of the observed TKE in essence indicates the vertical development of the fog layer but it is not captured by the model. This is a signature that the limited turbulence produced by the model results in the underestimation of the depth of the fog layer. After 08 UTC the modeled values are an overestimation of reality and, as will be discussed further in Section 4.2, this might be the reason for which the fog layer begins slightly dissipating before the observed one. The geostrophic wind in the forcing data, added to a 1D simulation without heterogeneous surface conditions, is not so detailed for a more correct simulation of the wind which is more complex in reality, and therefore the model is also unable to precisely reproduce the small-scale variations of TKE (Porson et al., 2011).

The model reproduces quite correctly the wind speed profiles in the lower boundary layer during the period of interest (Fig. 5b). Above, in the residual layer, due to the constant geostrophic wind forcing, an inertial oscillation is developing, inducing alternatively underestimation and overestimation of the wind speed. Sensitivity tests on the geostrophic wind (not shown) have shown that it does not impact the vertical extent of the fog layer and its microphysical characteristics.

4.2. Microphysical performance of the model

The understanding of the model's performance is enhanced by studying the model's ability to correctly reproduce microphysical characteristics such as the LWP, the LWC at 2.5 m agl and droplet size distributions. Taking into account the threshold of LWC = 0.05 gm^{-3} (Bergot et al., 2007) for the detection of the fog onset, and according to the LWC time-height evolution (Fig. 7a) the fog formation and dissipation times are 0150 and 0830 UTC, respectively. Therefore the modeled fog forms and dissipates half an hour and one hour in advance, respectively. Moreover, the simulated fog initially forms at the surface contrary to reality that forms at the level of 150 m agl. The height of the fog is underestimated since, during the observed fog event duration, it reaches 179 m height agl in contrast to the observed 300 m height. High LWC and N_c are produced from the fog onset up to its mature phase with values between 0.2 and
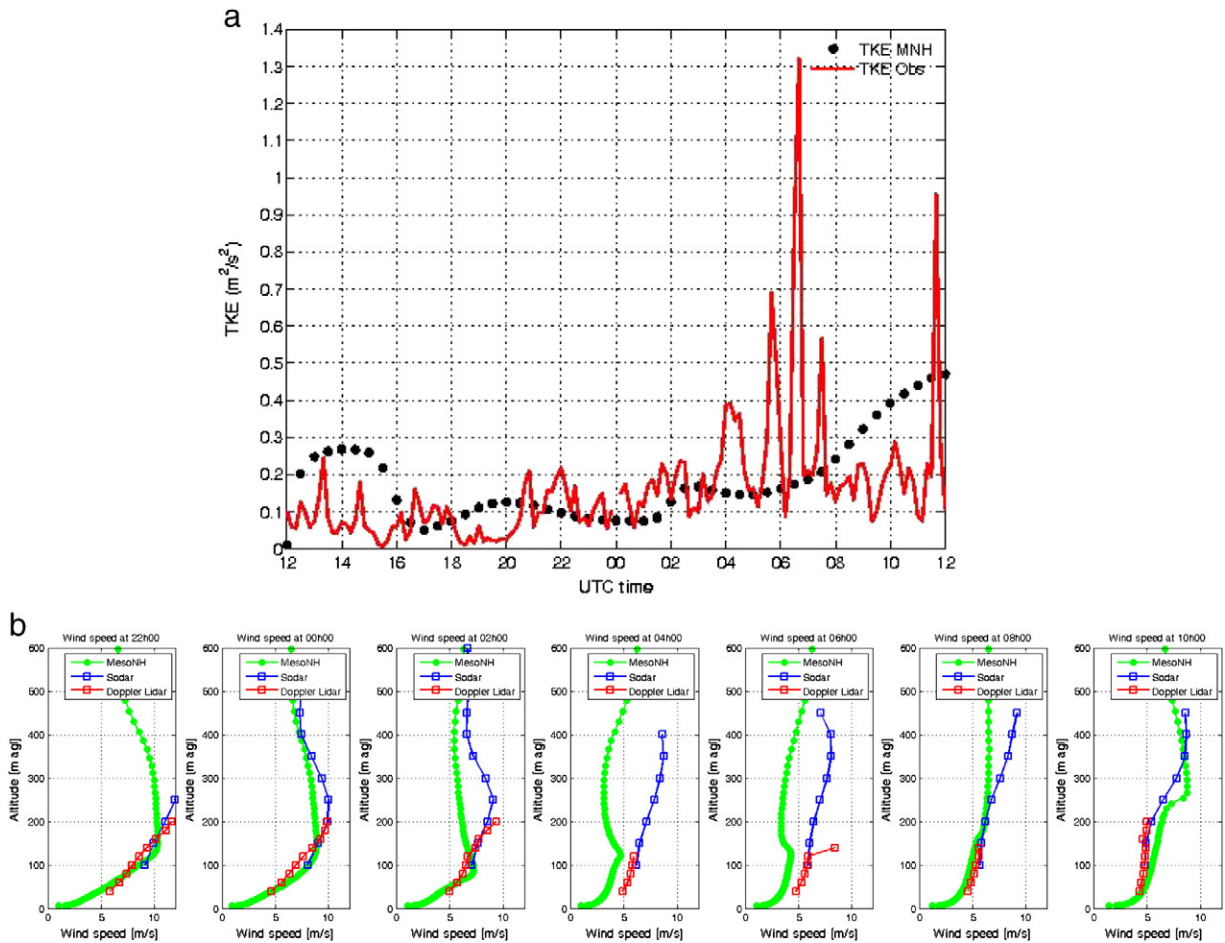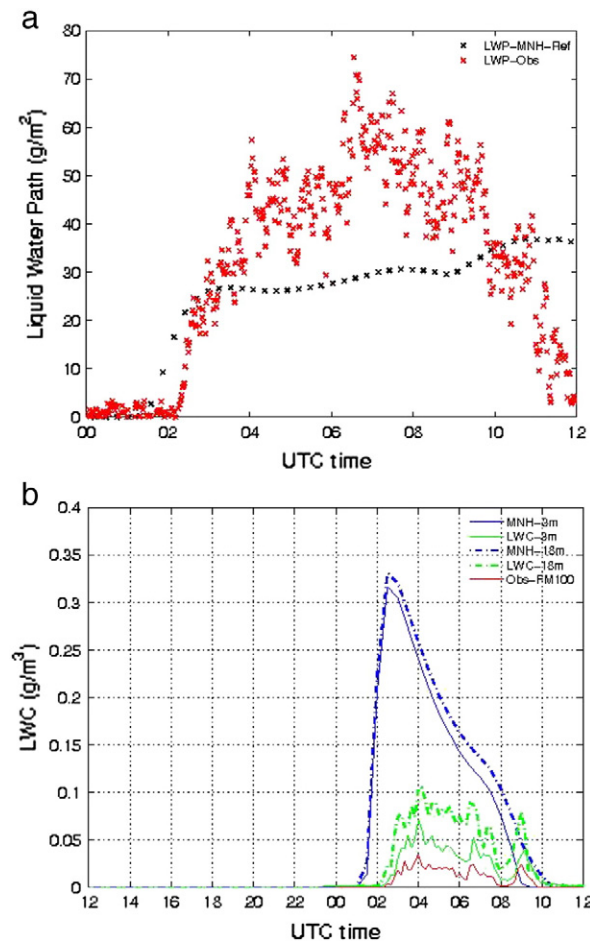
Fig. 5. (a) Temporal evolution of simulated and observed TKE ($m^2\ s^{-2}$) at 10 m agl; (b) temporal evolution of simulated and observed vertical profiles of wind speed. Profiles every 2 h from 22 UTC to 10 UTC. Height in m agl.

0.34 gm^{-3} and N_c up to 250 #cm^{-3} (Fig. 7b). LWC values are clearly overestimated near the ground compared to observations (Fig. 6b). This overestimation of LWC could be a result of the simulated fog initially forming at the surface compared to reality, where fog forms at a higher level. As soon as the modeled fog layer starts forming, CCN are activated and numerous droplets form that are too small to sediment, inducing too high values of LWC and N_c. Also, close to the ground larger values of N_c are recorded, while at the top N_c is substantially reduced. This agrees with what has been found from other researchers in observed situations according to which rapid temporal variations in droplet concentrations, sometimes with amplitudes corresponding to two orders of magnitude (Lu et al., 2013; Gerber, 1981, 1991), and LWC from near zero up to 0.5 gm^{-3} have been observed (Fuzzi et al., 1992). The core of the highest LWC values occurs before the mature phase between 02 and 03 UTC and lies between 28 and 34 m agl in the vertical, around 40 m close to the top of the fog layer. LWC and N_c increase with height up to the fog's top where they reach minimum values. Such a structure agrees with what has been found by several researchers (Pilié et al., 1975; Goodman, 1977; Pinnick et al., 1978) according to which the mean droplet diameter and liquid water content increased with height. When the fog lifts the ground N_c starts

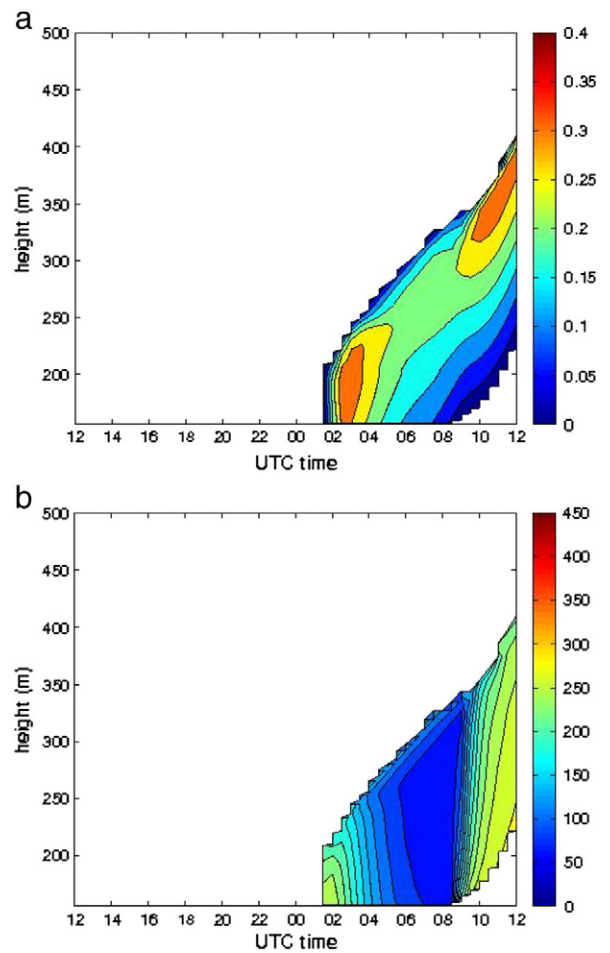increasing again indicating that the fog layer is transformed into a stratus cloud.

To shed more light on the overestimation of the LWC, we examined the LWC values and the liquid water profile as observed and simulated by the model. At 2.5 m agl (Fig. 6b) it is clear that there is a significant difference between the modeled and observed values (maximum modeled values of 0.32 gm^{-3} versus observed of 0.05 gm^{-3}). Concerning the liquid water profile we have superimposed the modeled LWC versus the LWC calculated using the visibility values at the two measurement levels (3 and 18 m agl) and Kunkel's formula (Kunkel, 1984). This way and in absence of other LWC measurements in the vertical we gain an insight into the LWC vertical gradients. According to Figs. 6c and 7a, the temporal change of LWC near the surface exhibits a gradual increase of values from the fog onset until 04 UTC and it starts decreasing again after that time point up to the end of the event. In the vertical LWC exhibits a smooth change with height between 0.1 and 0.35 gm^{-3}, in the first 70 m layer above which it has a decreasing trend up to the fog's top where its values reach minimal levels. On the contrary, observed values of LWC are lower than 0.05 gm^{-3} at the surface, they reach 0.1 gm^{-3} at 18 m agl height and reach about 0.2 gm^{-3} at the fog's top (300 m height) as deduced

Fig. 6. (a) Temporal evolution of simulated and observed LWP (gm^{-2}); (b) temporal evolution of observed LWC at 2.5 m agl as recorded by FM-100 (red thin line), simulated LWC at 3 m (green thin line) and at 18 m agl (blue thin line) and observed LWC calculated with visibility measurements at 3 m (green thick dashed dotted line) and 18 m agl (blue thick dashed dotted line) height. Reference run.

Fig. 7. (a) Time-height plot of LWC (gm^{-3}) and (b) droplet number concentration (N$_c$, #cm^{-3}). Reference run. Height in m above sea level (asl).

from the integrated LWP. Consequently there is a stronger vertical heterogeneity in observed LWC values in comparison with the modeled ones. Given the simulated and observed fog's layer height, the discrepancy in the LWC values at 2.5 m agl height and the heterogeneity of the values in the vertical, we conclude that added measurements of LWC in the vertical would be useful in order to explore the microphysical processes. Consequently, we will mainly base the following sensitivity study on the LWP values.

Fig. 6a represents the time series of the LWP as recorded by the HATPRO microwave radiometer and modeled by Meso-NH. The mean observed and modeled LWP during the mature phase of the fog event (between 04 and 08 UTC) are 49 gm^{-2} (standard deviation of 9 gm^{-2}) and 28 gm^{-2} (standard deviation of 2 gm^{-2}), respectively. Consequently the model underestimates the actual LWP as the fog layer is thinner than in reality. The optically thinner fog layer also explains the underestimation of LW radiative fluxes previously underlined, as the cooling of the fog's top is inhibited. Another

consequence is that mixing with warmer and drier air from the layer above the fog is missed, inducing the negative bias on surface temperature and positive bias on surface RH, as well as an underestimation of TKE near the ground. The modeled LWP values do not decrease after the dissipation of fog since the fog is lifted from the surface and it is transformed into a stratus cloud.

The simulated droplet size distribution at 2.5 m agl height has also been studied. The droplet size distribution in the model is described by the normalized form of the generalized gamma distribution which gives a monomodal form. Fig. 8 presents the observed (as recorded with FM-100) and modeled droplet size distributions shortly after onset (03 UTC), mature (06 UTC) and dissipation (08 UTC) phases of the fog life cycle. At 03 UTC the simulated droplet number concentration is higher (304 #cm^{-3}) than during the rest of the event, with droplets of 10 μm mean diameter, in contrast to the mature stage (06 UTC) during which droplets are larger (~12 μm) with lower number concentration (140 #cm^{-3}). At 08 UTC (dissipation stage) the droplets become again smaller in size (~10 μm). This temporal change in droplet size and in droplet number concentration follows the natural process, according to which in the beginning of the fog formation droplets are smaller, with higher concentration and as the fog layer matures, they become
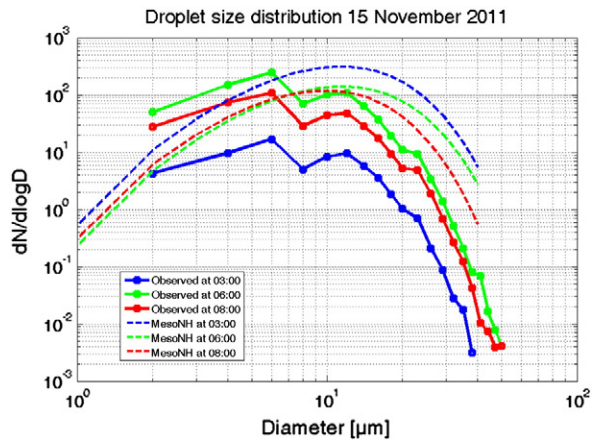
Fig. 8. Observed (FM-100) and modeled droplet size distribution at 03, 06 and 08 UTC. Reference run.

larger, with their concentration declining. The observed size distribution is bimodal and the second peak that corresponds to a ~13 μm droplet diameter size seems to be the mode corresponding to the modeled one. Thus the size of the modeled droplets is close to reality while, as previously mentioned, there is a discrepancy between the modeled and the observed values of the number concentration. Such a discrepancy is consistent with the overestimation of the modeled LWC.

The previous analysis on the model's performance shows that the 1D model on this particular fog event represents quite correctly the fog life cycle, with, however, an advance on the dissipation time. The discrepancies are more important on the vertical and temporal variability of the droplets, in terms of mass and number. The vertical extent of the fog is too low, underestimating the LWP. But droplet number concentration and LWC are overestimated near the ground, mainly at the onset of the fog, when droplets are too small to sediment. This underlines the complexity of fog microphysical processes. Therefore sensitivity tests on aerosol concentration and chemistry were conducted.

4.3. Sensitivity of fog characteristics to CCN number concentration and chemistry

4.3.1. CCN number concentration

Taking into account the previous results on the model's performance, sensitivity tests have been performed in order to examine whether and how fog characteristics such as LWP, droplet number concentration, visibility, onset and dissipation times, height, density are influenced by changes in the aerosols size distribution characteristics such as the CCN number concentration (N). Two tests have been performed: the N of the reference run (541 #cm^{-3}) is at first doubled (1082 #cm^{-3}, test TOTNX2) and second divided by two (270.5 #cm^{-3}, test TOTND2). According to Elias et al. (2014), in November 2011 at SIRTA, aerosol number concentration (independent of size) ranged from 6000 to 30000 cm^{-3} in dry conditions (visibility >5 km) that precede radiative fog formation. In mist conditions (5 km < visibility < 1 km) preceding fog formation, this concentration ranged from 5000 to 15000 cm^{-3}. This is an indication that the aerosol number

concentration can vary by a factor of 3–5 in conditions preceding radiative fog formation. Hence we design a sensitivity experiment where the concentration N ranges across a factor 4, by halving and doubling the reference case concentration.

Fig. 9a shows that during the mature phase of the fog event, when the CCN number concentration is doubled, the LWP also increases by on average 13 gm^{-2} in comparison to the reference run for the observed fog duration. The LWC comparisons with the reference run (not shown) show that fog becomes deeper by around 14 m. The time-height change of N$_c$ (Fig. 10a) provides more evidence showing that the fog's life-cycle is slightly affected, with the dissipation time occurring half an hour earlier. Around the fog onset, N$_c$ reaches a value of 467 #cm^{-3} at the surface, double the reference N$_c$. The time-height changes of the values follow the same pattern as for the reference run. The highest values of N$_c$ are recorded at the beginning of the fog formation decreasing gradually up to the mature phase (06 UTC). N$_c$ is higher near the ground and diminishes in the vertical up to the fog's top.
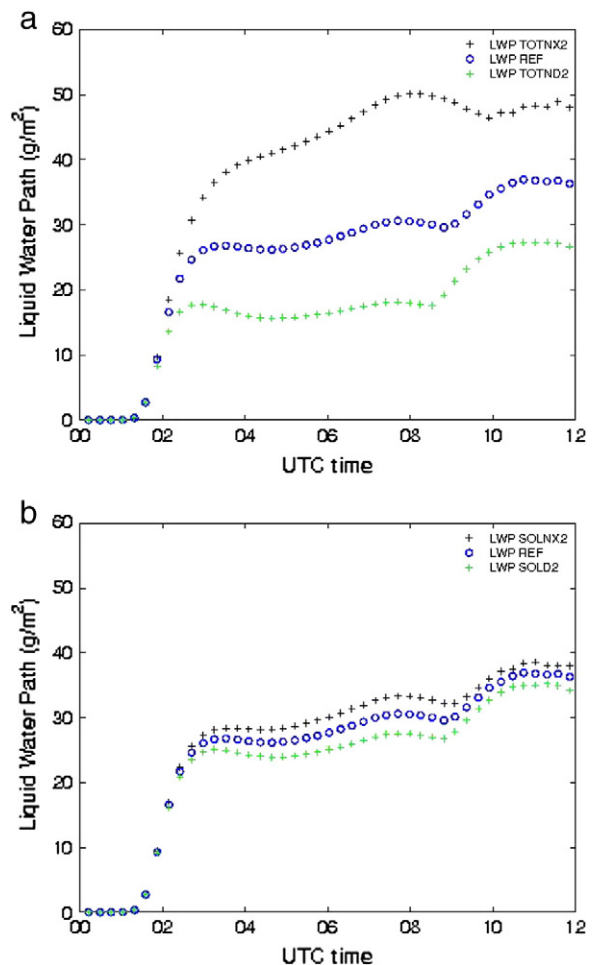

Fig. 9. a) 12-h time series of LWP (gm^{-2}) for the reference run (blue circle), TOTNX2 (black cross) and TOTND2 (green cross), b) the same as (a) but for tests SOLX2 (black cross) and SOLD2 (green cross).
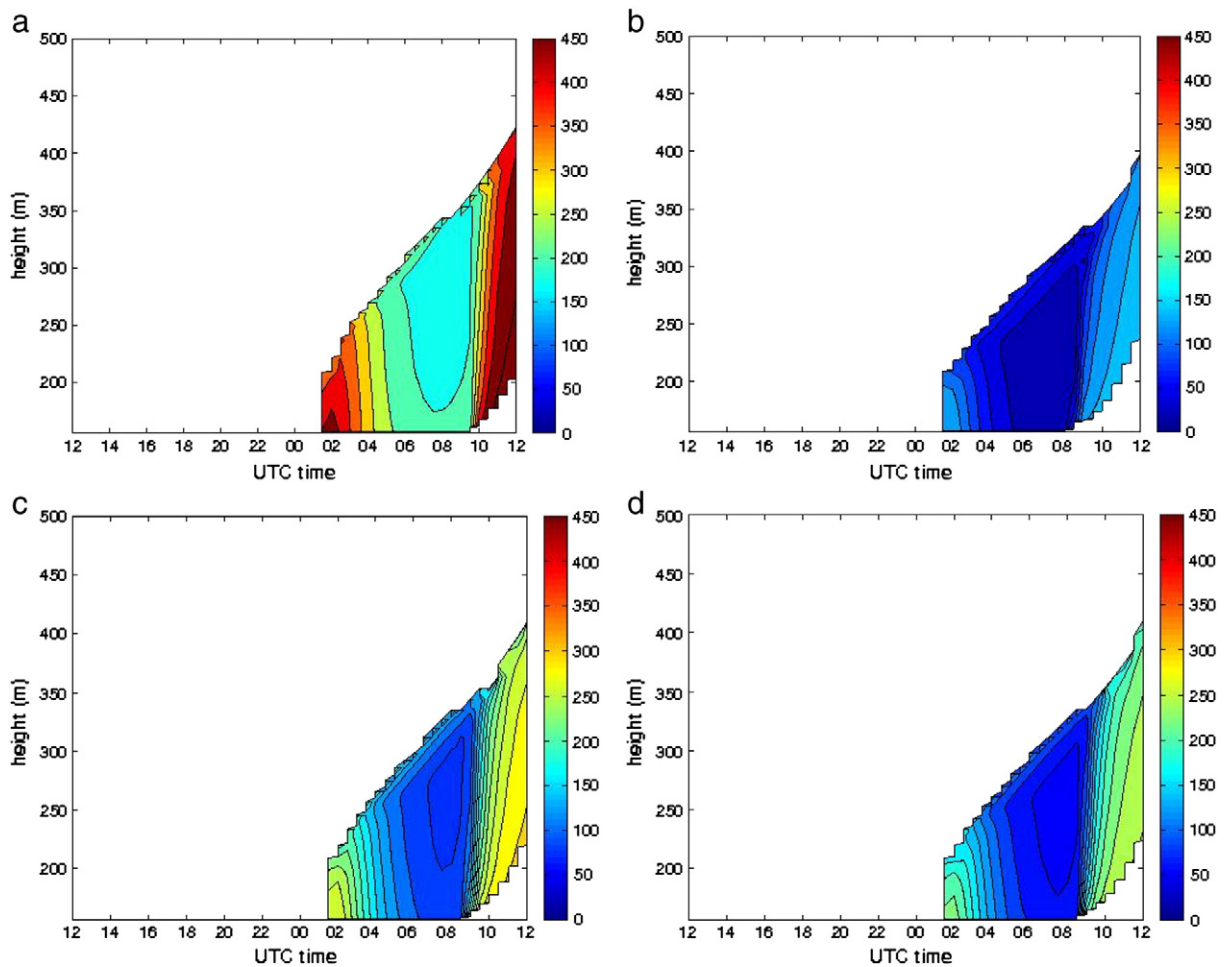
Fig. 10. Time-height plot of droplet number concentration (N_c, #cm^{-3}) for tests a) TOTNX2, b) TOTND2, c) SOLX2 and b) SOLD2. Height in m above sea level (asl).

The results of the TOTND2 test are relative to those of the previous one. The effects on LWP, LWC and N_c are opposite compared to the TOTNX2 test. LWP is clearly decreased by 40% (from 28 to 17 gm^{-2}) during the mature stage of the fog (Fig. 9a). However, the maximum values of LWC are quite close to the corresponding reference run values (0.30 versus 0.34 gm^{-3}). Although LWC still remains high, the effect of the decreased number of CCN is obvious. The influence of N on N_c is quite strong as shown in Fig. 10b. Since half of the original number of potentially activated aerosols exists, less aerosols are activated in forming droplets so N_c drops down to 150 # cm^{-3} at the onset time, about 40% in comparison to the reference run. Close to the end of the modeled fog event, the N_c is almost zero. Fog onset time is not affected but the dissipation time is shifted half an hour earlier than in the reference run. The height of the fog layer is also affected, decreasing by around 23 m in thickness.

4.3.2. Aerosol chemistry

Further tests have been performed in order to examine the influence of solubility on the fog characteristics. Solubility in the context of the Cohard et al. (1998) parameterization means the mass fraction of the aerosol soluble material over the total mass of the material (1: fully soluble and 0: totally insoluble). Internally mixed aerosols are considered with a chemical composition and solubility that do not depend on the size of the particles. No data regarding the solubility of the aerosols observed at SIRTA are available. An effort has been made for an estimation of it, taking into account the chemical composition of dry aerosols as provided by measurements of an Aerosol Chemical Speciation Monitor instrument (ACSM, Aerodyne, Billerca, MA) instrument installed at a distance of 5 km from the main SIRTA platform. According to Dupont et al. (2014, under review) as observed for 68 fog cases of the period 2010–2012, during the fog life cycle, on average, the dry aerosols are composed of 56% organic matter, 11% NH$_4^+$, 4% SO$_4^{2-}$, 28% NO$_3^-$ and 1% Cl$^-$. Here we hypothesize that for the period of 14/11 to 15/11/2011, the composition is similar, with organic material reaching 60%. We also make the hypothesis that the organic material is insoluble thus assuming that the solubility of the aerosols is 0.4. Therefore, the tests presented so far have been performed by setting the solubility of aerosols to 0.4. Solubility has been doubled (S = 0.8, test SOLX2) and divided by two (S = 0.2, test SOLD2) and the model's ability to produce the correct fog characteristics has been examined in two independent tests.

Fig. 9b presents the temporal change of the LWP for both tests along with the reference run. It is evident that throughout the simulation there is no significant difference between the reference and the two tests. Comparing SOLX2 and SOLD2 LWP values with the reference run we conclude that there is the same absolute difference ($3\ gm^{-2}$) in the mean for both runs. Also both runs simulate much less LWP than in reality, which is expected since the model underestimates LWP for this fog case study. The process behind the influence of solubility on the fog water is natural. The more soluble the material of the aerosols is (i.e. solubility = 0.8), the higher the optical thickness becomes, since more water is produced. On the opposite, a less soluble material induces less aerosol activation into fog droplets, therefore less water is produced. Notwithstanding, it is evident that the effect of solubility on the fog water is of the order of only 9% and less than the influence of the number of CCN.

The LWP changes due to the changes in solubility are produced by changes in droplet number concentration. There is a linear relationship between the solubility of the aerosol material and the droplet number concentration, since, the latter is increasing (decreasing) when solubility doubles (is halved) in relation to the reference run. However, the N_c of the two tests (SOLX2 and SOLD2) are quite similar, with subtle differences. Specifically in test SOLX2 (Fig. 10c) N_c reaches a maximum value of 279 #cm^{-3} close to the surface at dissipation time. The pattern that N_c follows through time and in the vertical is similar to that of the reference simulation. The same vertical and temporal change applies for test SOLD2 (Fig. 10d), while the values of N_c are around 17% less than in SOLX2. In comparison to the reference run these changes translate to almost the same 8–9% increase (decrease) of N_c. However it seems that solubility of the solid material of the aerosol does not exert an influence on the fog onset and dissipation times as deduced from the LWC values as well (not shown).

Table 2 summarizes the results of the sensitivity tests focusing on some fog features and microphysics parameters in order to obtain a better understanding and grasp of the changes that take place due to aerosol characteristics alterations. It is clear that the onset time is not affected by independently changing CCN number concentration or aerosol solubility but what changes is the dissipation time. For the latter, all simulations produce a fog layer that dissipates 1–1.5 h earlier than in reality. The introduction of a doubled (halved) N in the air mass translates into a 160% (65%) increase (decrease) in the production of fog droplets. Increased (reduced) number of droplets also induces a 60% (40%) increase (decrease) of the LWP. It also affects the thickness of the fog layer (fog height), while the LWC is increased (decreased) by 37% (32%). This outlines that the relationship between N_c and LWP or LWC is linear and positive. The aerosol influence is less pronounced on the fog's height which follows a smoother increase (decrease) of around 10% (4%). This is connected with the inherent limitations of the simulation presented in the previous section. The impact on the microphysical characteristics of the fog event are not significant either by introducing almost fully soluble aerosols (solubility = 0.8) or by introducing more insoluble ones (solubility = 0.2). Changes in LWP, LWC and N_c are of the same order of magnitude for both cases and they are in the order of 5%–17% depending on the microphysics parameter. The results of the aforementioned tests are also reflected on the estimated mean droplet radii of each case. As expected the biggest fog droplets are produced with the increase of the potentially activated aerosol concentration, while doubling or halving the solubility has almost no influence on the fog droplet radii. Still both factors affect fog microphysics characteristics and more work needs to be done for a more complete understanding of their respective role. It is also clear that by altering any of the two parameters, fog's height remains low, indicating the necessity of more detailed forcings that will produce more representative over the SIRTA site thermohygrometric, radiative and microphysical conditions.

5. Conclusions

A case of radiation fog that occurred at SIRTA Observatory has been extensively studied with the ultimate objective of shedding more light on the physical processes that took place during its life cycle and examining the influence of microphysics and aerosol characteristics on certain fog characteristics. This task was accomplished with in-situ and remote-sensing

Table 2

Summary of values of some aerosol characteristics (CCN number concentration and solubility), fog characteristics (onset and dissipation time, height) and microphysics parameters (LWP, LWC, droplet number concentration, mean droplet radius) from the sensitivity study: Observed (for comparison), REF, TOTNX2, TOTND2, SOLX2, SOLD2.

	OBS	REF	TOTNX2	TOTND2	SOLX2	SOLD2
CCN number concentration (#cm^{-3})	541	541	1082	270.5	541	541
Aerosols solubility	0.4	0.4	0.4	0.4	0.8	0.2
Fog onset time (UTC)	02	0145	0145	0145	0145	0145
Fog dissipation time (UTC)	0930	0830	0910	0800	0830	0800
LWP (gm^{-2}, 06 UTC)	53.4	27.7	44.4	16.5	30.1	23.0
Fog top height (m) (06 UTC)	300	142	156	136	142	142
LWC (gm^{-3}) (06 UTC, 45 m asl)	0.015[1]	0.19	0.26	0.13	0.20	0.18
Droplet number concentration (#cm^{-3}) (06 UTC, 45 m asl)	80[1]	81	214	28	95	68
Mean droplet radius (μm) (06 UTC, 45 m asl)	3.55[2]	8.24	6.62	10.35	7.95	8.58

[1] At 2.5 m agl.

[2] These values are calculated and derived with the formula: $LWC = \frac{4}{3}\pi\rho Nr^3$.

observations and with the 1D mode of the Meso-NH model. The analysis on the model's performance versus observations shows that the model, for this particular fog event, represents quite correctly the fog life cycle, with an advance on the dissipation time. The main discrepancy is a limitation of the vertical extent of the fog by 60% (120 m), probably due to insufficiently detailed large scale forcings. The data of the forcings are derived from radiosondes that are taken 15 km West of SIRTA, their temporal resolution is low, while the measurements at SIRTA that could be used for this case are limited to low levels, close to the surface. The direct consequence of these limitations is an underestimation of the LWP that limits the cooling at the top of the fog layer. Therefore the mixing at the cloud top, entraining warmer and dryer air from above to the lower levels, is inhibited. This results in an underestimation of the TKE and temperature near the surface and an overestimation of humidity. Consequently the LWC and the droplet number concentration are overestimated near the ground, mainly at the onset of the fog, when droplets are too small to sediment. Another reason for the LWC overestimation can be the fact that fog is forming at a different height in the simulation compared to reality, i.e. at the surface versus aloft. All these underline the necessity to add detailed and frequent in-situ observations of temperature, relative humidity and microphysics profiles using tethered balloons in order to improve the forcings and also to better document the microphysical properties. Such measurements can be quite a challenge.

The influence of some aerosol characteristics on fog life cycle was further studied. The sensitivity tests revealed that, in the reference run, the approach followed to represent the aerosol characteristics in the aerosol activation spectra parameterization of the model, based on actual observations, gives satisfactory results. The CCN number concentration exerts a higher influence on the fog microphysical characteristics than chemistry (solubility) does. Doubling or halving the solubility produces similar results on the water and N_c produced, on the duration of the fog and its height and they are very close to the reference conditions. For both factors, the duration of the fog event is mainly affected at the end of the event and is of the order of up to 1.5 h. Fog height is also sensitive to changes in CCN concentration (N), with the changes being in the order of around 35%, while doubling (halving) the N translates to an almost double (half) LWP and a more striking influence on the production of droplets. In the case of doubled N, the LWP values reach the observed ones and although this shows a better approximation to reality, it is translated into an even higher overestimation of LWC and N_c that the model produces in the reference simulation.

These results underline the complexity of the fog microphysical processes and the challenge to improve mainly microphysics schemes in order to improve the representation of the vertical variability (and the horizontal one in a 3D framework, considering surface heterogeneities) aiming at improving the forecast and at better understanding the physical processes. The work presented has shown that future efforts should entail an improvement of the two-moment microphysics scheme with the aim of performing sensitivity studies with a configuration of the model where the vertical structure of thermo-hygrometric, dynamic, and radiative parameters are represented in a more realistic manner.

References

Abdul-Razzak, H., Ghan, S.J., 2000. A parameterization of aerosol activation 2. Multiple aerosol types. J. Geophys. Res. 105 (D5), 6837–6844.

Abdul-Razzak, H., Ghan, S.J., Rivera-Carpio, C., 1998. A parameterization of aerosol activation 1. Single aerosol type. J. Geophys. Res. 103 (D6), 6123–6131.

Bergot, T., 2012. Small-scale structure of radiation fog: a large-eddy simulation study. Q. J. R. Meteorol. Soc. 139, 1099–1112.

Bergot, T., Terradellas, E., Cuxart, J., Mira, A., Liechti, O., Mueller, M., Nielsen, N.W., 2007. Intercomparison of single-column numerical models for the prediction of radiation fog. J. Appl. Meteorol. Climatol. 46, 504–521.

Bott, A., 1991. On the influence of the physico-chemical properties of aerosols on the life-cycle of radiation fogs. Bound.-Layer Meteorol. 56, 1–31.

Bott, A., Carmichael, G.R., 1993. Multiphase chemistry in a microphysical radiation fog model—a numerical study. Atmos. Environ. 27A, 503–522.

Bott, A., Sievers, U., Zdunkowski, W., 1990. A radiation fog model with a detailed treatment of the interaction between radiative transfer and fog microphysics. J. Atmos. Sci. 47, 2153–2166.

Bougeault, P., Lacarrére, P., 1989. Parameterization of orography-induced turbulence in a meso-beta scale model. Mon. Weather Rev. 117, 1872–1890.

Cohard, J.-M., Pinty, J.-P., 2000. A comprehensive two-moment warm microphysical bulk scheme. Part I: description and selective tests. Q. J. R. Meteorol. Soc. 126, 1815–1842.

Cohard, J.-M., Pinty, J.-P., Bedos, C., 1998. Extending Twomey's analytical estimate of nucleated cloud droplet concentrations from CCN spectra. J. Atmos. Sci. 55, 3348–3357.

Cohard, J.-M., Pinty, J.-P., Suhre, K., 2000. On the parameterization of activation spectra from CCN microphysical properties. J. Geophys. Res. 105 (D9), 11753–11766.

Cuxart, J., Jiménez, M.A., 2012. Deep radiation fog in a wide closed valley study by numerical modelling and remote sensing. Pure Appl. Geophys. 169, 911–926.

Cuxart, J., Bougeault, P., Redelsperger, J.-L., 2000. A turbulence scheme allowing for mesoscale and large-eddy simulations. Q. J. R. Meteorol. Soc. 126, 1–30.

Dabas, A., Remy, S., Bergot, T., 2011. Use of a sodar to improve the forecast of fogs and low clouds on airports. Pure Appl. Geophys. 169, 769–781.

Dupont, J.-C., Haeffelin, M., Protat, A., Bouniol, D., Boyouk, N., Morille, Y., 2012. Stratus fog formation and dissipation. A 6-day case study. Bound.-Layer Meteorol. 143, 207–225.

Duynkerke, P.G., 1991. Radiation fog: a comparison of model simulation with detailed observations. Mon. Weather Rev. 119, 324–341.

Duynkerke, P.G., 1999. Turbulence, radiation and fog in Dutch stable boundary layers. Bound.-Layer Meteorol. 90, 447–477.

Eldridge, R.G., 1966. Haze and fog distributions. J. Atmos. Sci. 23, 605–613.

Elias, T., Haeffelin, M., Drobinski, P., Gomes, L., Rangognio, J., Bergot, T., Chazette, P., Raut, J.-C., Colomb, M., 2009. Particulate contribution to extinction of visible radiation: pollution, haze, and fog. Atmos. Res. 92, 443–454.

Fisher, E.L., Caplan, P., 1963. An experiment in the numerical prediction of fog and stratus. J. Atmos. Sci. 20, 425–437.

Foote, G.B., Toit, P.S.Du., 1969. Terminal velocity of raindrops aloft. J. Appl. Meteorol. 8, 249–253.

Fuzzi, S., Facchini, M.C., Orsi, G., Lind, J.A., Wobrock, W., Kessel, M., Maser, R., Jaeschke, W., Enderle, K.H., Arends, B.G., Berner, A., Solly, A., Kruisz, C., Reischl, G., Pahl, S., Kaminski, U., Winkler, P., Ogren, J.A., Noone, K.J., Hallberg, A., Fierlinger-Oberlinninger, H., Puxbaum, H., Marzorati, A., Hansson, H.-C., Wiedensohler, A., Svenningsson, I.B., Martinsson, B.G.,

Schell, D., Georgii, H.W., 1992. The Po Valley Fog Experiment 1989. An overview. Tellus 44B, 448–468.

Fuzzi, S., Laj, P., Ricci, L., Orsi, G., Heintzenberg, J., Wendisch, M., Yuskiewicz, B., Mertes, S., Orsini, D., Schwanz, M., Wiedensohler, A., Stratmann, F., Berg, O.H., Swietlicki, E., Rank, G., Martinson, B.G., Günther, A., Diersen, J.P., Schell, D., Jaeschke, W., Berner, A., Dusek, U., Galambos, Z., Kruisz, C., Mesfin, N.S., Wowbrock, W., Arends, B., Ten, B.H., 1998. Overview of the Po Valley fog experiment 1994 (CHEMDROP). Contrib. Atmos. Phys. 71, 3–19.

Geoffroy, O., Brenguier, J.-L., Sandu, I., 2008. Relationship between drizzle rate, liquid water path and droplet concentration at the scale of a stratocumulus cloud system. Atmos. Chem. Phys. 8, 4641–4654.

Gerber, H.E., 1981. Microstructure of a radiation fog. J. Atmos. Sci. 38, 454–458.

Gerber, H., 1991. Supersaturation and droplet spectral evolution in fog. J. Atmos. Sci. 48, 2569–2588.

Goodman, J., 1977. The microstructure of California coastal fog and stratus. J. Appl. Meteorol. 16 (10), 1056–1067.

Guedalia, D., Bergot, T., 1994. Numerical forecasting of radiation fog. Part II: a comparison of model simulations with several observed fog events. Mon. Weather Rev. 122, 1231–1246.

Gultepe, I., Tardif, R., Michaelides, S.C., Cermak, J., Bott, A., Bendix, J., Müller, M.D., Pagowski, M., Hansen, B., Ellrod, G., Jacobs, W., Toth, G., Cober, S.G., 2007. Fog research: a review of past achievements and future perspectives. Pure Appl. Geophys. 164, 1121–1159.

Gultepe, I., Pearson, G., Milbrandt, J.A., Hansen, B., Platnick, S., Taylor, P., Gordon, M., Oakley, J.P., Cober, S., 2009. The fog remote sensing and modeling field project. Bull. Am. Meteorol. Soc. 90, 341–359.

Haeffelin, M., Bergot, T., Elias, T., Tardif, R., Carrer, D., Chazette, P., Colomb, M., Drobinski, P., Dupont, E., Dupont, J.-C., Gomes, L., Musson-Genon, L., Pietras, C., Plana-Fattori, A., Protat, A., Rangognio, J., Raut, J.-C., Rémy, S., Richard, D., Sciare, J., Zhang, X., 2010. PARISFOG, shedding new light on fog physical processes. Bull. Am. Meteorol. Soc. 91, 767–782.

Haeffelin, M., Dupont, J.C., Boyouk, N., Baumgardner, D., Gomes, L., Roberts, G., Elias, T., 2013. A comparative study of radiation fog and quasi-fog formation processes during the ParisFog field experiment 2007. Pure Appl. Geophys. 1–21 (May 2013. Available online at http://dx.doi.org/10.1007/s00024-013-0672-z).

Khairoutdinov, M., Kogan, Y., 2000. A new cloud physics parameterization in a large-eddy simulation model of marine stratocumulus. Mon. Weather Rev. 128, 229–243.

Kunkel, B.A., 1984. Parameterization of droplet terminal velocity and extinction coefficient in fog models. J. Clim. Appl. Meteorol. 23, 34–41.

Lafore, J.P., Stein, J., Asencio, N., Bougeault, P., Ducrocq, V., Duron, J., Fisher, C., Héreil, P., Mascart, P., Pinty, J.-P., Redelsperger, J.-L., Richard, E., Vilá-Guerau de Arellano, J., 1998. The Meso-NH atmospheric simulation system. Part I: adiabatic formulation and control simulation. Ann. Geophys. 16, 90–109.

Lillis, D., Cruz, C.N., Collett, J., Richards, W.L., Pandis, S.N., 1999. Production and removal of aerosol in a polluted fog layer: model evaluation and fog effect on PM. Atmos. Environ. 33, 4797–4816.

Liu, D.Y., Niu, S.J., Yang, J., Zhao, L.J., Lü, J.J., Lu, C.S., 2012. Summary of a 4-year fog field study in Northern Nanjing, Part 1: fog boundary layer. Pure Appl. Geophys. 169, 809–819.

Lu, C., Liu, Y., Niu, S., Zhao, L., Yu, H., Cheng, M., 2013. Examination of microphysical relationships and corresponding microphysical processes in warm fogs. Acta Meteorol. Sin. 27, 832–848.

Meyer, M.B., Lala, G.G., 1986. FOG-82: a cooperative field study of radiation fog. Bull. Am. Meteorol. Soc. 65, 825–832.

Mlawer, E., Taubman, S.J., Brown, P.D., Ianoco, M., Clough, S.A., 1997. Radiative transfer for inhomogeneous atmospheres: RRTM a validated correlated-k model for the longwave. J. Geophys. Res. 102, 16663–16682.

Morcrette, J.-J., 1991. Radiation and cloud radiative properties in the ECMWF operational weather forecast model. J. Geophys. Res. 96 (D5), 9121–9132.

Morille, Y., Haeffelin, M., Drobinski, P., Pelon, J., 2007. STRAT: an automated algorithm to retrieve the vertical structure of the atmosphere from single-channel lidar data. J. Atmos. Ocean. Technol. 24 (5), 761–775.

Müller, M.D., Masbou, M., Bott, A., 2010. Three-dimensional fog forecasting in complex terrain. Q. J. R. Meteorol. Soc. 136, 2189–2202.

Musson-Genon, L., 1987. Numerical simulation of a fog event with one-dimensional boundary layer model. Mon. Weather Rev. 115, 592–607.

Noilhan, J., Planton, S., 1989. A simple parameterization of land surface processes for meteorological models. Mon. Weather Rev. 117, 536–549.

Pagowski, M., Gultepe, I., King, P., 2004. Analysis and modelling of an extremely dense fog event in southern Ontario. J. Appl. Meteorol. 43, 3–16.

Pal, S., Haeffelin, M., Batchvarova, E., 2013. Exploring a geophysical process based attribution technique for the determination of the atmospheric boundary layer depth using aerosol lidar and near surface meteorological measurements. J. Geophys. Res. Atmos. 118 (16), 9277–9295.

Philipona, R., Kräuchi, A., Romanens, G., Levrat, G., Ruppert, P., Brocard, E., Jeannet, P., Ruffieux, D., Calpini, B., 2013. Solar and thermal radiation errors on upper-air radiosonde temperature measurements. J. Atmos. Ocean. Technol. 30, 2382–2393.

Pilié, R.J., Mack, E.J., Kocmond, W.C., Rogers, C.W., Eadie, W.J., 1975. The life cycle of valley fog. Part I: micrometeorological characteristics. J. Appl. Meteorol. 14, 347–363.

Pinnick, R.G., Hoihjelle, D.L., Fernandez, G., Stenmark, E.B., Lindberg, J.D., Hoidale, G.B., 1978. Vertical structure in atmospheric fog and haze and its effects on visible and infrared extinction. J. Atmos. Sci. 35, 2020–2032.

Porson, A., Price, J., Lock, A., 2011. Radiation fog. Part II: large-eddy simulation in very stable conditions. Bound.-Layer Meteorol. 139, 193–224.

Price, J., 2011. Radiation fog. Part I: observations of stability and drop size distributions. Bound.-Layer Meteorol. 139, 167–191.

Pruppacher, H., Klett, J., 1997. Microphysics of Clouds and Precipitation, first ed. Kluwer Academic Publishers, Massachusets.

Rangognio, J., Tulet, P., Bergot, T., Gomes, L., Thouron, O., Leriche, M., 2009. Influence of aerosols on the formation and development of radiation fog. Atmos. Chem. Phys. Discuss. 9 (5), 17963–18019.

Roach, W.T., 1976. On the effect of radiative exchange on the growth by condensation of a cloud or fog droplet. Q. J. R. Meteorol. Soc. 102 (432), 361–372.

Román-Cascón, C., Yagüe, C., Sastre, M., Maqueda, G., Salamanca, F., Viana, S., 2012. Observations and WRF simulations of fog events at the Spanish Northern Plateau. Adv. Sci. Res. 8, 11–18.

Seinfeld, J., Pandis, S., Pilinis, C., 1992. Heterogeneous sulfate production in an urban fog. Atmos. Environ. 26A, 2509–2522.

Shi, C., Wang, L., Zhang, H., Zhang, S., Deng, X., Li, Y., Qiu, M., 2012. Fog simulations based on multi-model system: a feasibility study. Pure Appl. Geophys. 169, 941–960.

Squires, P., 1958. The microstructure and colloidal stability of warm clouds. Part II—the causes of the variations in microstructure. Tellus 10, 262–271.

Squires, P., Twomey, S., 1960. The relation between cloud droplet spectra and the spectrum of cloud nuclei. Physics of Precipitation. Geophys. Monogr. Ser., vol. 5. AGU, Washington, D. C.

Tardif, R., Rasmussen, R.M., 2007. Event-based climatology and typology of fog in the New York City region. J. Appl. Meteorol. Climatol. 46 (8), 1141–1168.

Twomey, S., 1959. The nuclei of natural cloud formation. Part II: the supersaturation in natural clouds and the variation of cloud droplet concentration. Pure Appl. Geophys. 43, 243–249.

Van der Velde, I.R., Steeneveld, G.J., Wichers Schreur, B.G.J., Holtslag, A.A.M., 2010. Modeling and forecasting the onset and duration of severe radiation fog under frost conditions. Mon. Weather Rev. 138, 4237–4253.